A Study of Liquid Droplet Disintegration for the Development of Nanostructured Coatings

H. Tabbara

School of Engineering Sciences, University of Southampton, Highfield, Southampton, SO17 1BJ, U.K.

S. Gu

School of Engineering, Cranfield University, Cranfield, Bedfordshire, MK43 0AL, U.K.

Xi'an Jiaotong-Liverpool University, Suzhou Dushu Lake Higher Education Town, Suzhou 215123, China

Thermal spray coatings produced from a liquid feedstock are receiving an increasing level of interest due to the advanced, nanostructured coatings which are obtainable by these processes. In this article, a high-velocity oxy-fuel (HVOF) thermal spray system is computationally investigated to make a scientific assessment of the liquid droplet behavior on injection. An existing liquid-fuelled HVOF thermal spray gun is simulated using the computational fluid dynamic approach. The steady-state gas-phase dynamics are initialized by the introduction of liquid kerosene and oxygen which react within the combustion chamber producing a realistic compressible, turbulent jet. Discrete-phase water droplets are injected at the powder injection port. On injection, the water droplets breakup and vaporize, while being entrained through the acceleration barrel of the HVOF system. The results obtained give an insight to the mechanism which control the water droplet sizes and disintegration process, and serve as a fundamental reference for future development of liquid feedstock devices. © 2012 American Institute of Chemical Engineers *AIChE J*, 58: 3533–3544, 2012
Keywords: coating flows, complex fluids, computational fluid dynamics, particulate flows, particle technology

Introduction

Thermal spray coatings are formed by accelerating a stream of molten, semimolten, or solid powder particles toward a targeted substrate where the particles initially undergo impact deformation and then adhere to the surface through diffusion-type bonds and mechanical interlocking. Then, the particles impinge onto one another, building up the coating particle by particle in a lamellar structure. A variety of different techniques can be used to heat and accelerate the particles, and can include a combination of plasma arc,[1] high-pressure inert gases,[2,3] and a combustion reaction.[4] As a result, a wide spectrum of particle impact velocities and temperatures can be achieved; ranging from several tens to several thousands of meters per second and from below room-temperature up to several thousand degrees Kelvin. Using these methods, almost every type of material that does not degrade when heated can be deposited to form a coating.

Thermally sprayed coatings are typically formed to protect a component against wear and corrosion, and in some cases create low-friction surfaces. Furthermore, new advanced functional surfaces are evolving in conjunction with thermal spray processing. Two interesting and topical examples include: the dye-sensitized solar cell[5] and functionally gradient prosthetic coatings with antibacterial components.[6] As

part of the high level of interest in more complex thermal spray coatings, there is a growing desire to deposit nanostructured films. However, the deposition of ultrafine submicron and nanosized particles requires current techniques to be adapted. For both health and safety reasons as well as to avoid particle agglomeration during storage and feeding into the spray device, a nanopowder feedstock has to be mixed to form a suspension (suspension thermal spraying, STS) or a solution precursor (solution precursor thermal spraying, SPTS). The liquid injection method also increases the momentum of the feedstock particles, aiding penetration into the thermal jet core. The consistently high levels of interest in the fields of STS and SPTS in recent years is reflected by the number of review papers published.[7–11] In all, a variety of thermal spray methods have been used in pursuit of depositing nanoparticles from a liquid feedstock, including: plasma, flame, and high-velocity oxy-fuel (HVOF). An overview of theses achievements is provided as follows.

Hydroxyapatite (HA), TiO_2, and Al_2O_3 are some of the most popular materials being deposited with the plasma spray method. Their respective functions include: prosthetics coatings, photocatalytic devices, and wear and corrosion protection. SPTS of HA using a plasma torch can produce fine splat morphologies, and demonstrates superior control of coating porosity, which is a key feature of prosthetic coatings.[12] The deposition of TiO_2 nanoparticles using liquid feedstock plasma spraying has been successfully achieved with grain sizes of roughly 40 nm, and with a high proportion (90%) of desirable anatase phase; vital in the production
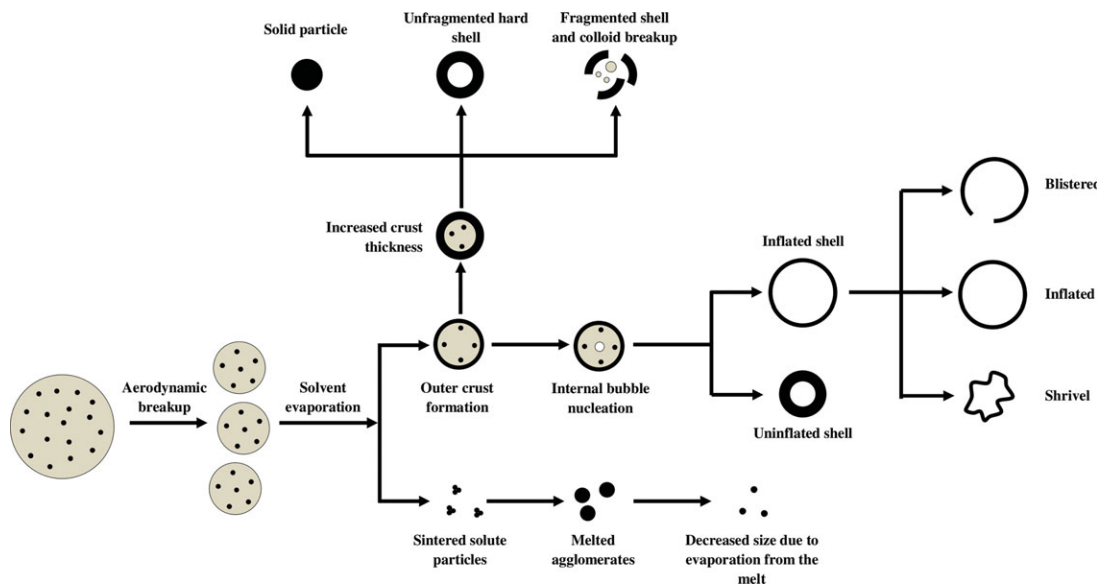
Figure 1. Variations in liquid feedstock droplet disintegration and drying.

[Color figure can be viewed in the online issue, which is available at wileyonlinelibrary.com.]

of photocatalytically active coatings.[13] Liquid feedstock alumina has also been deposited by plasma spraying with controlled coating density and with high levels of thermodynamically stable corundum (α-Al$_2$O$_3$), which is necessary for good wear resistance and electrical insulation.[14]

The flame spray method with liquid feedstock injection has been used for both manufacturing[15–17] and depositing TiO$_2$ nanometric particles. SPTS of TiO$_2$ using flame spray have successfully created nanostructured coatings, consisting of 80%[18] and 95%[19] anatase phase. However, cohesion between particles and their adhesion to the substrate can be limited. The high-velocity suspension flame spray method, based on existing HVOF technology, has shown a high level of potential for the deposition of submicron and nanosized particles due to its high momentum throughput and controllable flame characteristics, which can be used to improve the particle impact conditions. As a result, dense TiO$_2$ coatings with good adhesion to the substrate have been formed.[20] Furthermore, Al$_2$O$_3$ nanosized particles can be completely melted by this process, resulting in little interlamellar defects and extremely low interconnected porosity.[21] The liquid feedstock HVOF method has also been applied to experimentally manufacture Ceria-based electrolytes for solid-oxide fuel cells, where the flame limits the evaporation and decomposition of the feedstock compared to plasma spray alternatives, producing a low-porosity, smooth and defect free coating.[22]

In comparison to the conventional thermal spray methods, STS and SPTS are more complex due to the final particle morphology being largely controlled by the rates of fragmentation and vaporization of the liquid component of the feedstock on injection. Detailed images of the initial disintegration of liquid feedstock injection are provided in Ref. 23, exhibiting stripping and catastrophic breakup of the droplets. Depending on the size of the liquid droplets, the intensity of the flow and the liquid feedstock properties, the droplets may precipitate their solid mass along one of many process routes, as depicted in Figure 1. A simulation study of liquid ceramic precursor droplets processed by plasma and HVOF spraying are presented,[24,25] providing some explanation to the different precipitation routes. These results show smaller feedstock droplets form a thicker precipitate shell and are more likely to form solid particles due to rapid heating and vaporization. Larger droplets, however, undergo surface precipitation forming a shell. Depending on its porosity and ability to vent the evaporating liquid core, this shell structure can erupt due to internal pressurization. Furthermore, the temperatures associated with HVOF are lower than plasma spray methods, leading to larger particle diffusion times within feedstock droplets and, therefore, are more likely to produce thick shell and solid uniform agglomerates.[25]

Experiments using modified HVOF thermal spraying with a liquid feedstock indicate that if the feedstock is water based, poorer coatings might be created due to insufficient flame temperatures when mixing within the combustion chamber.[26] However, the water-based feedstock allows higher particle concentrations, are less expensive to produce, and are safer to handle compared with the organic alternatives.[27] Better coatings have been obtained when the feedstock is a combustible, organic-based compound. However, injecting a combustible liquid into the combustion chamber raises the pressure and can lead to instabilities in the flow.[9]

Despite the work undertaken to date in the fields of STS and SPTS, several investigations are still very necessary to improve our fundamental understanding of spray kinematics, suspension and solution feedstock properties, and injection systems. This study investigates liquid droplet disintegration within a supersonic combustion flame, based on HVOF-type processing. A good overview of the combustion characteristics and supersonic flow field within the JP5000 have been previously documented.[28,29] The reader may also refer to literature[30,31] for detailed simulation-based investigations concerning micron sized powder particles and process gas interactions in cold gas spraying and HVOF, respectively. The work presented within the latter example applies multiscale modeling by combining steady-state combustion, particulate phase dynamics and heating, and rule-based stochastic methods, leading to the prediction and control of detailed and accurate coating microstructures.[31–33]
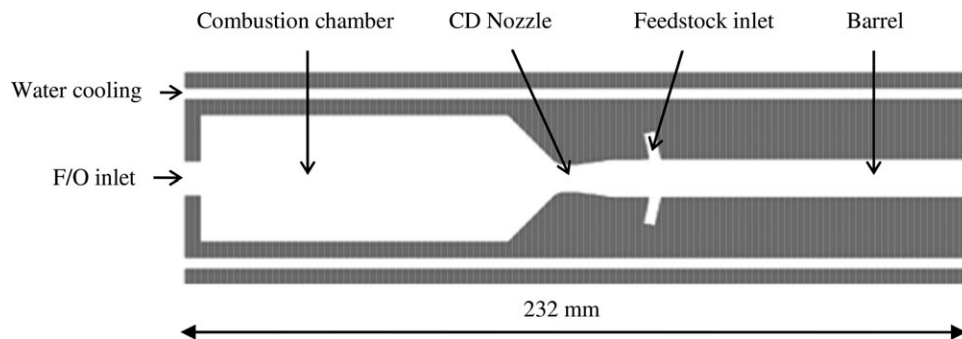
Figure 2. Schematic diagram of the JP5000 thermal spray system.

In this investigation, a commercial finite volume computational fluid dynamic code, user-defined functions, and an equilibrium combustion reaction program are combined to simulate the flow field through the most widely used liquid-fuelled HVOF thermal spray system, JP5000 (Praxair). The water droplets at room-temperature and various sizes are introduced at the normal powder feeder location. Then, a detailed study is conducted to assess the manner of droplet disintegration within the barrel of a standard HVOF system, close to the de Laval nozzle. By incorporating detailed thermophysical properties of water, the primary and secondary breakup regimes are captured and compared to the timescales involved with those of vaporizing droplets. The information obtained sheds new light on the process of water droplet disintegration and serve as a reference for future development of liquid feedstock devices.

Model Description

An overview of the gas-phase modeling techniques

A schematic diagram of the JP5000 thermal spray system is illustrated in Figure 2 highlighting the fuel-oxygen inlet, the combustion chamber, the convergent–divergent nozzle, and the barrel. The position of the powder feeder is also shown. A mixture of fuel and oxygen is injected into the combustion chamber through the central inlet. The feedstock powder particles are introduced downstream of the convergent–divergent nozzle using a carrier gas. The axisymmetric gun design can be well represented by a 2-D simulation domain which is adopted in this study. Details of the computation domain, boundary conditions, and refinement regions are given in previous studies.[28,29] The geometric parameters and the working conditions for the simulation are summarized in Table 1 and are based on values provided by industry.

The segregated solution algorithm[34] is applied in this study with a control volume-based technique. This numerical method is chosen over the alternative coupled approach to aid convergence and avoid oscillations in the pressure and velocity fields. The pressure and velocity fields are linked using the semi-implicit method for pressure linked equations algorithm[35,36] due to it being computationally economical and more stable in comparison to other algorithms. The second-order upwind scheme is used to discretize the transport equations.

The steady-state flow field of the gaseous continuum is computed using the Reynolds averaged Navier–Stokes equations and is assumed to behave as a compressible, ideal gas. The absolute pressure is represented by the sum of the operating pressure and the static pressure of the flow. The variable density is calculated by taking into account the mass fraction of each species in the flow as given in Eq. 1.

$$\rho = \frac{p_{op} + p}{RT \sum_i \frac{Y_i}{M_{o,I}}} \tag{1}$$

The continuity equation for the steady state, axisymmetric computations is given by Eq. 2. The terms on the left hand side represent the mass entering and leaving a control volume and the change in mass due to a change in density. The S_m term is the additional mass contribution from the vaporizing kerosene fuel droplets, where x is the axial coordinate, r is the radial coordinate, v_x is the axial velocity, and v_r is the radial velocity. The individual water droplets are the focus of this study and are injected as single droplets to make particular assessment of individual droplet behavior. These droplets are one way coupled, therefore, do not impact on the gas-phase dynamics.

$$\frac{\partial}{\partial x}(\rho v_x) + \frac{\partial}{\partial r}(\rho v_r) + \frac{\rho v_r}{r} = S_m \tag{2}$$

The axial and radial momentum conservation equations are given in Eqs. 3 and 4 in their cylindrical form. The effective viscosity is equal to the sum of the physical dynamic viscosity and the artificial turbulent viscosity, which is used to account for the enhanced mixing due to turbulent fluctuations within the mean flow. The flow in this case is compressible; hence,

Table 1. A summary of Geometric Parameters and the Working Conditions Based on the Industrial Setup

Geometric Parameter		Working Conditions	
Barrel length	111.1 mm	Fuel	Flow rate: 0.0057 kg/s Temperature: 300 K
Barrel entrance diameter	11.0 mm	Oxygen	Flow rate: 0.022 kg/s Temperature: 300 K
Barrel exit diameter	11.1 mm	Atmosphere	Pressure: 101325 Pa Temperature: 300 K
Combustion chamber length	92.5 mm	Internal wall boundary	Temperature: 350 K Nonslip
Combustion chamber diameter	37.8 mm		
Nozzle throat diameter	7.9 mm		

the two equations below are Favre averaged. The radial and axial sources F_r and F_x represent the volumetric forces due to interaction with the dispersed kerosene fuel droplets.

$$\frac{1}{r}\frac{\partial}{\partial x}(r\rho v_x v_x) + \frac{1}{r}\frac{\partial}{\partial r}(r\rho v_r v_x) =$$
$$-\frac{\partial p}{\partial x} + \frac{1}{r}\frac{\partial}{\partial x}\left[r\mu_{\text{eff}}\left(2\frac{\partial v_x}{\partial x} - \frac{2}{3}(\Delta \cdot \vec{v})\right)\right]$$
$$+ \frac{1}{r}\frac{\partial}{\partial r}\left[r\mu_{\text{eff}}\left(\frac{\partial v_x}{\partial r} + \frac{\partial v_r}{\partial x}\right)\right] + F_x \quad (3)$$

$$\frac{1}{r}\frac{\partial}{\partial x}(r\rho v_x v_r) + \frac{1}{r}\frac{\partial}{\partial r}(r\rho v_r v_r) =$$
$$-\frac{\partial p}{\partial r} + \frac{1}{r}\frac{\partial}{\partial x}\left[r\mu_{\text{eff}}\left(\frac{\partial v_r}{\partial x} - \frac{\partial v_x}{\partial r}\right)\right]$$
$$+ \frac{1}{r}\frac{\partial}{\partial r}\left[r\mu_{\text{eff}}\left(2\frac{\partial v_r}{\partial r} - \frac{2}{3}(\nabla \cdot \vec{v})\right)\right]$$
$$- 2\mu_{\text{eff}}\frac{v_r}{r^2} + \frac{2}{3}\frac{\mu_{\text{reff}}}{r}(\nabla \cdot \vec{v}) + F_r \quad (4)$$

where

$$\nabla \cdot \vec{v} = \frac{\partial v_x}{\partial r} + \frac{\partial v_r}{\partial r} + \frac{v_r}{r} \quad (5)$$

The energy conservation equation is given below, and is linked to the conservation of mass and momentum through the multispecies ideal gas law (Eq. 1). The source term S_h represents the energy dissipated and received by the gas phase during the vaporization and exothermic combustion reaction of the kerosene fuel droplets within the combustion chamber.

$$\frac{\partial}{\partial x}[v_x(\rho E + p)] + \frac{\partial}{\partial r}[v_r(\rho E + p)] = \frac{\partial}{\partial x}(v_x \sigma_{xx} + v_r \tau_{xr} + q_x)$$
$$+ \frac{\partial}{\partial x}(v_x \tau_{xr} + v_r \sigma_{rr} + q_r) + S_h \quad (6)$$

where

$$\sigma_{xx} = 2\mu_{\text{eff}}\frac{\partial v_x}{\partial x} - \frac{2}{3}\mu_{\text{eff}}(\nabla \cdot \vec{v}) \quad (7)$$
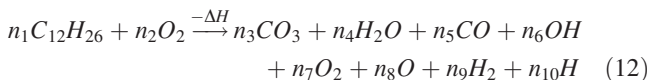
$$\sigma_{rr} = 2\mu_{\text{eff}}\frac{\partial v_r}{\partial r} - \frac{2}{3}\mu_{\text{eff}}(\nabla \cdot \vec{v}) \quad (8)$$

$$\tau_{xr} = \tau_{rx} = \mu_{\text{eff}}\left(\frac{\partial v_x}{\partial r} + \frac{\partial v_r}{\partial x}\right) \quad (9)$$

$$q_x = K_{\text{eff}}\frac{\partial T}{\partial x} \quad (10)$$

$$q_r = K_{\text{eff}}\frac{\partial T}{\partial r} \quad (11)$$

The kerosene liquid fuel, $C_{12}H_{26}$, in this study is used to represent the average size of the kerosene hydrocarbon chain. The combustion reaction is represented by a single, one-step global reaction scheme, as given in Eq. 12.

$$n_1 C_{12}H_{26} + n_2 O_2 \xrightarrow{-\Delta H} n_3 CO_3 + n_4 H_2O + n_5 CO + n_6 OH$$
$$+ n_7 O_2 + n_8 O + n_9 H_2 + n_{10} H \quad (12)$$

The eddy-dissipation model[37] is adopted to predict the rate of combustion reaction between kerosene and oxygen. This method is a turbulence–chemistry interaction model, where the

rate ($R_{i,r}$) at which species i is produced due to reaction r, is given by the limiting value of Eqs. 13 and 14. An iterative approach is used[4] to estimate the mole fraction of each product species appearing on the right hand side of Eq. 12, to achieve the correct combustion chamber pressure and thermal flow field.

$$R_{i,r} = v'_{i,r} M_{\omega,i} A\rho \frac{\varepsilon}{k} \min_R \left(\frac{Y_R}{v'_{R,r} M_{\omega,R}}\right) \quad (13)$$

$$R_{i,r} = v'_{i,r} M_{\omega,i} AB\rho \frac{\varepsilon}{k} \left(\frac{\sum_P Y_P}{\sum_J^N v''_{j,r} M_{\omega,j}}\right) \quad (14)$$

The k-ε model[38] is the most frequently used turbulence model in computing flows within a practical engineering environment. The model assumes that the turbulent viscosity of the flow is isotropic and the flow is fully turbulent. One of the main downfalls of the standard k-ε model is its inability to accurately predict the spreading rate of an axisymmetric planar jet. This problem was thought to originate within the equation of turbulent dissipation. Hence, the realizable k-ε model[39] addresses this by containing a modified transport equation to describe the rate of turbulent dissipation. Equations 15 and 16 describe the transport of turbulent kinetic energy and the rate of turbulent dissipation.

$$\frac{\partial}{\partial r}(r\rho k v_r) + \frac{\partial}{\partial x}(r\rho k v_x) = \frac{\partial}{\partial x}\left(r\left(\mu + \frac{\mu_t}{\sigma_\kappa}\right)\frac{\partial k}{\partial x}\right)$$
$$+ \frac{\partial}{\partial r}\left(r\left(\mu + \frac{\mu_t}{\sigma_\kappa}\right)\frac{\partial k}{\partial r}\right) + r(G_k + G_b - \rho\epsilon - Y_M) \quad (15)$$

$$\frac{\partial}{\partial x}(r\rho\varepsilon v_x) + \frac{\partial}{\partial r}(r\rho\varepsilon v_r) = \frac{\partial}{\partial r}\left(r\left(\mu + \frac{\mu_t}{\sigma_\varepsilon}\right)\frac{\partial\varepsilon}{\partial r}\right)$$
$$+ \frac{\partial}{\partial x}\left(r\left(\mu + \frac{\mu_t}{\sigma_\varepsilon}\right)\frac{\partial\varepsilon}{\partial x}\right)$$
$$+ r\left(\rho C_1 S\varepsilon - \rho C_2 \frac{\varepsilon^2}{k + \sqrt{v\varepsilon}} + \rho C_{1\varepsilon}\frac{\varepsilon}{k}C_{2\varepsilon}G_b\right) \quad (16)$$

The realizable model also considers the requirement of a more complete description of the normal stresses, which makes the model physically more complete. The normal stress is by definition, positive and to satisfy this requirement C_μ is made variable in relation to the mean flow and the turbulence, as defined in Eq. 17. Then, the variable C_μ is directly applied to estimate the tubulent viscosity μ_t.

$$C_\mu = \frac{1}{A_0 + A_s(kU^*/\varepsilon)} \quad (17)$$

Droplet Dynamics with Heat and Mass Transfer

Spherical, discrete-phase water droplets are injected vertically into the barrel at the standard powder inlet port, as shown in Figure 2. The acceleration of each droplet particle is calculated using Newton's second law, equating the inertia of each droplet with the forces applied by the continuum, described by Eq. 18.

$$\frac{du_p}{dt} = \frac{18\mu}{\rho_p d_p^2}\frac{C_D Re_p}{24}(v - u_p) + F_t \quad (18)$$

Subsequently, the trajectory of each droplet is tracked by computing its displacement through time. F_t is a source term which accounts for the thermophoretic force. This force arises

due to temperature gradients within the flow. As outlined in previous studies,[40] in particle laden flows where the relative Mach number M_r exceeds 0.6 shock patterns form on the particle surface. Therefore, the calculation of the particle drag force should include both the particle Reynolds number and the relative Mach number. For this reason, the drag force coefficient C_D is calculated using the model proposed by Henderson,[41] as given in Eqs. 19–21.

IF $M<1$:

$$C_D = 24\left[Re + S\left\{4.33\left(\frac{3.65 - 1.53\frac{T_p}{T}}{1 + 0.353\frac{T_p}{T}}\right) \times exp\left(-0.247\frac{Re}{S}\right)\right\}\right]^{-1}$$
$$+ exp\left(-\frac{0.5M}{\sqrt{Re}}\right)\left[\frac{4.5 + 0.38(0.03Re + 0.48\sqrt{Re})}{1 + 0.03Re + 0.48\sqrt{Re}} + 0.1M^2 + 0.2M^8\right] + \left[1 - exp\left(-\frac{M}{Re}\right)\right]0.6S \quad (19)$$

IF $M > 1.75$:

$$C_D = \frac{0.9 + \frac{0.34}{M_\infty^2} + 1.86\left(\frac{M_\infty}{Re_\infty}\right)^{0.5}\left[2 + \frac{2}{S_\infty^2} + \frac{1.058}{S_\infty}\left(\frac{T_p}{T}\right)^{0.5} - \frac{1}{S_\infty^4}\right]}{1 + 1.86\left(\frac{M_\infty}{Re_\infty}\right)^{0.5}}$$

(20)

IF $1<M<1.75$:
$$C_D(M_\infty, Re_\infty) = C_D(1, Re_\infty)$$
$$+ \frac{4}{3}(M_\infty - 1)[C_D(1.75, Re_\infty) - C_D(1, Re_\infty)] \quad (21)$$

The droplet temperature during heating and vaporization is governed by Eq. 22. The convective heat-transfer coefficient between each droplet and the gaseous phase in which they are submersed is calculated using the Ranz–Marshall correlation[42,43] given in Eq. 23. The variation in specific heat capacity with temperature for liquid water is applied using data presented in the literature.[44]

$$m_p c_p \frac{dT_p}{dt} = hA_p(T_\infty - T_p) + \frac{dm_p}{dt}h_{fg} \quad (22)$$

$$Nu = \frac{hd_p}{K_\infty} = 2.0 + 0.6Re_p^{\frac{1}{2}}Pr^{\frac{1}{3}} \quad (23)$$

During vaporization, the reduction of the droplet's mass begins to reduce in accordance to Eq. 24. If N_i is negative, and hence, the droplet temperature is lower than the dew point a condensation conditions would exist. In this instance, N_i is set to zero, and the droplet will undergo inert heating and cooling. The vapor concentration at the droplet outer surface $C_{i,s}$ is calculated by assuming that the vapor partial pressure is equivalent to its saturation vapor pressure, P_{sat} at T_p. The relationship between the temperature of the droplet T_p and the saturation vapor pressure $P_{sat}(T_p)$ is calculated using the well-known Clapeyron–Clausius relation.[45]

$$m_p(t + \Delta t) = m_p(t) - N_i A_p M_{\omega,i}\Delta t \quad (24)$$

where,

$$N_i = k_c(C_{i,s} - C_{i,\infty})$$

$$C_{i,s} = \frac{p_{sat}(T_p)}{RT_p}$$

$$C_{i,\infty} = X_i \frac{p}{RT_\infty}$$

The mass-transfer coefficient is evaluated through the Sherwood number correlation,[42,43] given by Eq. 25. The diffusion coefficient is calculated using the binary diffusion relation provided by Ref. 46, whereby the average molecular weight of the gas phases is calculated using the mass-fraction of each gaseous species within the gas phase surrounding the vaporizing droplet.

$$k_c = \frac{D_{i,m}}{d_p}\left(2.0 + 0.6Re_p^{\frac{1}{2}}Sc^{\frac{1}{3}}\right) \quad (25)$$

Droplet breakup

For the simulation of primary droplet breakup, the wave breakup model[43] is applied which simulates the stripping breakup mechanism. This model is appropriate for high speed applications, where $We > 100$, as defined in Eq. 26. The model considers the breakup of the droplets due to the relative velocity between the gas and liquid phases creating Kelvin–Helmholtz instabilities. The model assumes that the time of breakup and the resulting droplet sizes are related to the fastest growing Kelvin–Helmholtz instabilities at the droplet surface, where the droplet–gas interface exists.

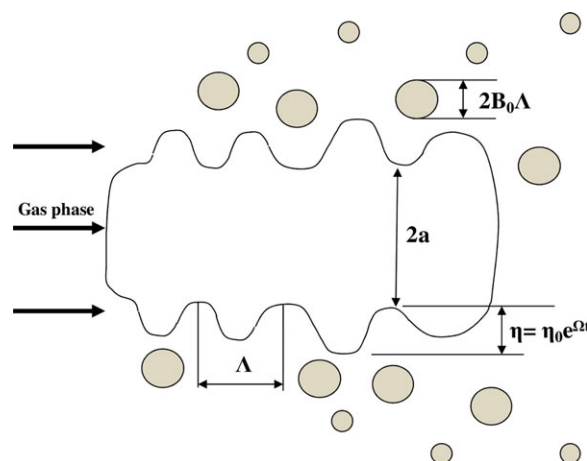$$We = \frac{\rho_\infty V_{rel}^2 d_p}{\sigma} \quad (26)$$

Figure 3. Diagram showing surface wave and breakup mechanism on a liquid blob droplet.

[Color figure can be viewed in the online issue, which is available at wileyonlinelibrary.com.]

The droplet breakup is simulated by assuming the radius of the child droplets is proportional to the wavelength of the fastest growing unstable surface wave on the parent droplet, as described by Eq. 27, and depicted in Figure 3, where B_0 is a model constant equal to 0.61.[47] The maximum growth rate, Ω, and its corresponding wavelength, Λ, are estimated by Eqs. 28 and 29, respectively.

$$r_p = B_0 \Lambda \tag{27}$$

$$\Omega = \frac{(0.34 + 0.38 We_2^{1.5})}{(1 + Oh)(1 + 1.4 Ta^{0.6})} \left(\frac{\rho_1 a^3}{\sigma}\right)^{-1} \tag{28}$$

$$\Lambda = 9.02 a \frac{(1 + 0.45 Oh^{0.5})(1 + 0.4 Ta^{0.7})}{(1 + 0.8 We_2^{1.67})^{0.6}} \tag{29}$$

The rate of change of droplet radius of the parent droplet is calculated by Eq. 30, where the breakup time τ is given in Eq. 31. The model constant B_1 is tested for values of 1 and 10. Variations in viscosity and surface tension with temperature for the liquid water droplets are applied using data correlations from the literature, respectively.[48,49]

$$\frac{da}{dt} = -\frac{(a - r_p)}{\tau_p} \tag{30}$$

$$\tau_p = \frac{3.726 B_1 a}{\Lambda \Omega} \tag{31}$$

For the secondary droplets whose We are far less than 100, the Taylor analogy breakup (TAB) model is applied. This approach is based on Taylor's analogy[50] between an oscillating and distorting droplet and a spring mass system. When the oscillations of the parent droplet grow to a critical value, break up occurs, and several smaller droplets are created. The criterion for droplet break up is based on the distortion ratio. The nondimensional mass, spring, damper system for the calculation of droplet distortion is given in Eq. 32, where break up occurs if $y > 1$.

$$\ddot{y} = \frac{C_F}{C_b} \frac{\rho_g}{\rho_p} \frac{V_{rel}^2}{r_p^2} - \frac{C_k \sigma}{\rho_p r_p^3} - \frac{C_d V_{rel}}{\rho_p r_p^2} \dot{y} \tag{32}$$

The droplet oscillation frequency and the undamped oscillation amplitudes are calculated using Eqs. 33 and 34. Breakup is only possible if the condition in Eq. 35 is met.

$$A = \sqrt{(y^n - We_c)^2 + \left(\frac{(dy/dt)^n}{\omega}\right)^2} \tag{33}$$

$$\omega^2 = C_k \frac{\sigma}{\rho_l r^3} = \frac{1}{t_d^2} \tag{34}$$

$$We_c + A > 1 \tag{35}$$

If this condition is met, the breakup time is calculated based on the time required for y to equal unity. If the breakup time is greater than the droplet time at the next droplet time step then breakup will not occur during the current time step, and y and (dy/dt) are updated accordingly. Conversely, if the current and next droplet time steps are less than and greater than the droplet breakup time, respectively, breakup will occur. The child droplet radii are determined by Eq. 36, which is derived by equating the energy of the parent droplet to the combined
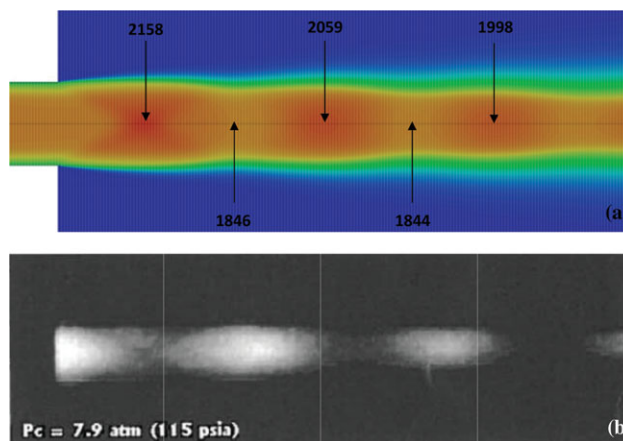
Figure 4. Comparison between simulated gas-phase velocity contours (ms^{-1}) (a) and an experimental image[51] (b) of the under expanded flow regime at the JP5000 barrel exit.

[Color figure can be viewed in the online issue, which is available at wileyonlinelibrary.com.]

energy of the child droplets.

$$r_{32} = \frac{r}{1 + \frac{8 Z y^2}{20} + \frac{\rho_p r^3 (dy/dt)^2}{\sigma} \left(\frac{6Z - 5}{120}\right)} \tag{36}$$

The empirical constants applied for the wave breakup model and TAB model are based on recommended values, and the predicted breakup times and child droplet sizes compare well to experimental observations, as presented later in this investigation.

Results and Discussion

Gas-phase dynamics summary

The steady state, compressible flow field through the HVOF thermal spray system is captured based on the industrial fuel and oxygen injection flow rates, as listed in Table 1. The simulated velocity distribution at the barrel exit is compared with experimental observations[51] in Figure 4, with the simulated under expanded jet structure showing a good physical likeness. The flame temperature within the combustion chamber is compared to the expected values for varying equivalence ratios in Figure 5a, and the temperature variations at the exit of the barrel are also compared to experimental measurements[52] in Figure 5b, both showing good concordance.

The process is initialized by injecting liquid fuel droplets into the combustion chamber with pure oxygen gas where they heat, evaporate, and then exothermically combust, creating a highly pressurized gaseous mixture at a maximum flame temperature of 3377 K. The simulated exhaust gas mixture consisting of O, O_2, H, H_2, OH, H_2O, CO_2, and CO exits the combustion chamber. At the convergent–divergent nozzle, the gas is rapidly accelerated. At the throat of the convergent–divergent nozzle, the flow is choked at Mach one. Two small discontinuities follow as the gas expands and accelerates through the divergent section, marked by slight increases in velocity along the centerline. These flow characteristics are described by the interlinked gas velocity, temperature, and pressure along the centerline as depicted in Figure 6. Several shocks occur through the barrel due to the
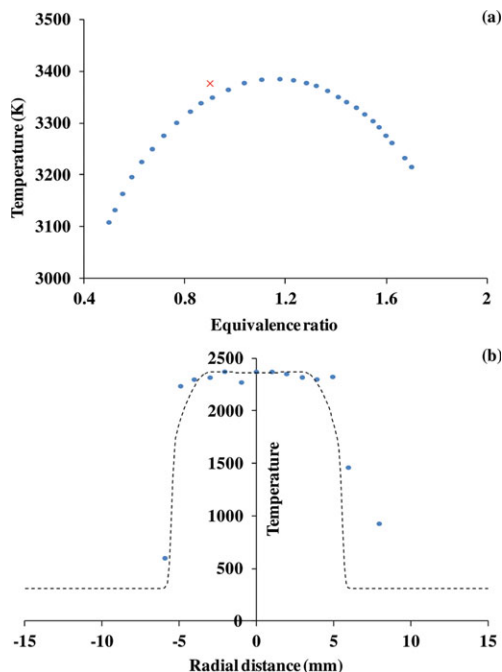
Figure 5. Graph showing the flame temperature variation for changes in equivalence ratio[52] (a) and comparison between point measured temperatures[52] and modeled temperature distribution at the exit of the barrel (b).

[Color figure can be viewed in the online issue, which is available at wileyonlinelibrary.com.]

expansion of the supersonic gas and strong reflections at the solid internal surface of the barrel. An under-expanded flow regime at the exit of the barrel is present, enforced by a slightly subcritical atmospheric back pressure. The fluctuations in flow properties at the exit of the barrel are created by the flow periodically over expanding and then reconverging above and below atmospheric pressure. These adjustments continually overshoot due to the boundary communicating with the jet by sound waves, which naturally travel slower than the bulk supersonic flow.

Droplet investigation

Water droplets are injected vertically into the barrel at the powder inlet port 0.138 m from the combustion chamber back wall, as depicted in Figure 2. Their initial droplet velocity is 20 ms^{-1}, and this process is repeated for droplet sizes varying between 50 and 500 μm. First, the droplets are simulated to breakup without vaporization as predicted by the wave breakup model. Figure 7 describes the modeled linear decrease in a 50-μm parent droplet diameter as the child droplets are shed from its surface. The modeling constant B_1 is set to both 1 and 10. These values represent a lower and upper limit of this coefficient and directly control the rate at which the droplet breaks up (Eq. 31). The time taken for the 50-μm parent droplet to completely breakup is, therefore, estimated to be between 2.2 μs and 16.5 μm. This process is repeated for increasing droplet sizes, and the time taken for each parent droplet to shed all of its mass is plotted in Figure 8 for both values of B_1. For the 500-μm parent droplet this time may, therefore, be between 17 and 115 μs.

Figure 9a plots the converging size of the child droplets during the breakup process with initial parent droplet diameters varying from 50 to 500 μm, as predicted by the wave breakup model. The dimensionless time in this graph represents the total time from injection of the initial parent droplet divided by the time taken for the initial parent droplet to completely disintegrate (see Figure 8) with a B_1 value of unity. Because of the continuing decrease in child droplet size beyond a dimensionless time of 1, it is clear a secondary atomization process is simulated. The primary droplets are filtered from the data presented in Figure 9a and are plotted in Figure 9b. The results indicate that the initial primary child droplets are roughly 4.5–4.6 μm for all the tested parent droplets. The data obtained also indicates that as the initial parent droplet size is increased from 50 to 500 μm, the average primary child droplet size decreases. Consequently, the minimum primary droplet size obtained is 2.3 μm for the 500 μm parent droplet.

Figure 10 describes the rate of evaporation and decrease in droplet diameter of a 50-μm droplet without breakup being modeled. The results indicate that a 50-μm diameter droplet only decreases by 6 μm in a time of 0.5 ms, at which point the parent droplet reaches the exit of the computational domain. Furthermore, the decrease in particle diameter due to evaporation within the time taken for the 50 μm droplet
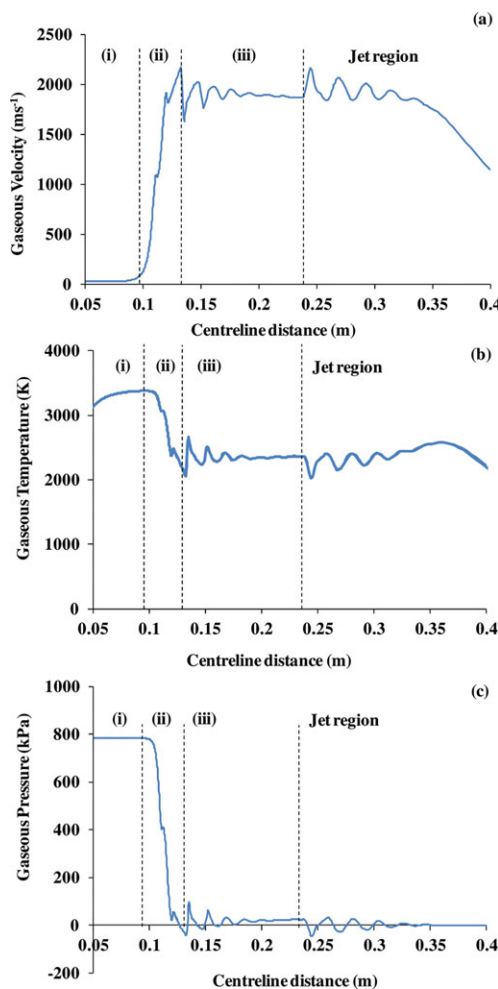
Figure 6. Variations in gaseous velocity (a), temperature (b), and pressure (c) along the centerline of the simulated HVOF torch.

[Color figure can be viewed in the online issue, which is available at wileyonlinelibrary.com.]
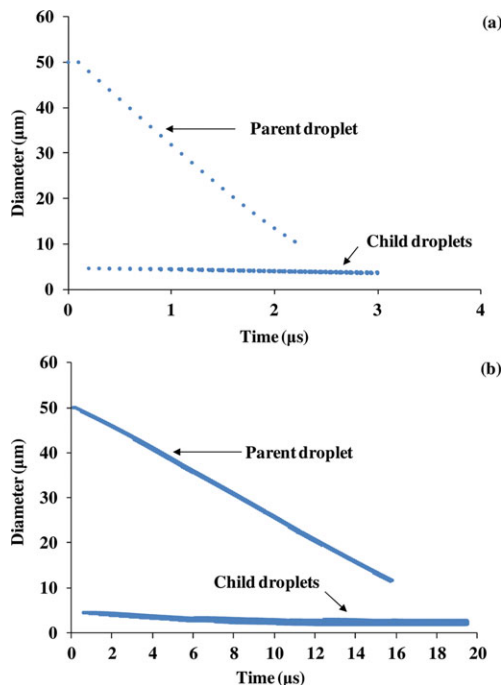
Figure 7. Graph describing the rate of decrease in 50 μm droplet diameter and the child droplet sizes for B_1 values of 1 (a) and 10 (b).

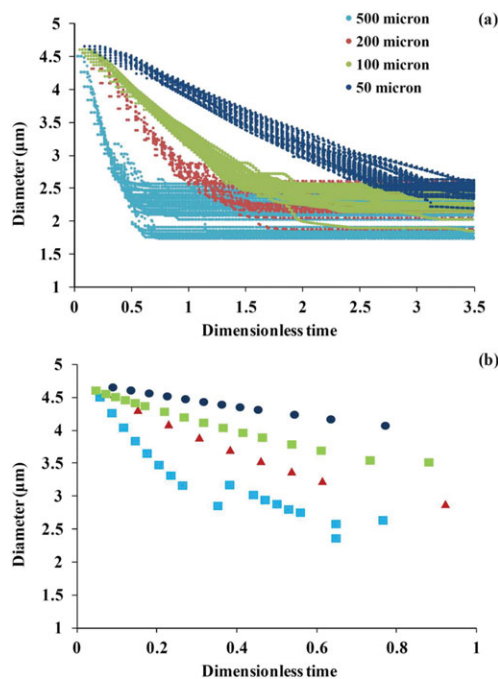[Color figure can be viewed in the online issue, which is available at wileyonlinelibrary.com.]

to shed its mass during breakup (i.e., between 2.2 μs to 16 μm) is at most 0.03%. From these result, it is clear that the primary droplet break up regimes for the tested parent droplets occur on a much smaller time scale compared to the vaporization process.

Figure 11 plots the times taken for a range of smaller sized droplets to decrease their mass by 10% due to vaporization alone, and also the time taken for these droplets to completely disintegrate due to breakup predicted by the TAB model. The initial displacement, velocity, and temperature of these droplets are representative of the droplets emitted by the wave breakup model. As the results suggest, for a 10-μm droplet the evaporation time far exceeds the breakup time. As the droplet size is decreased, these timescales become more comparable. When the droplet diameter is
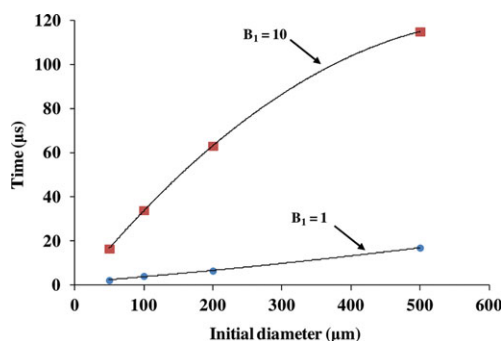
Figure 8. Graph comparing the time required for different sized initial parent droplets to shed all their mass. Both sets of data for B_1 values of 1 and 10 are presented.

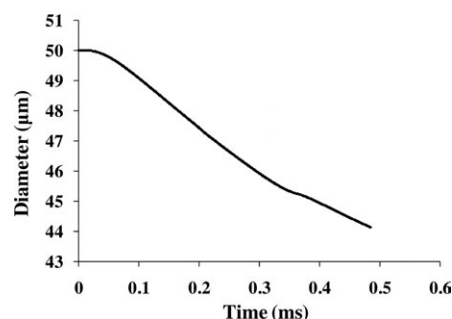[Color figure can be viewed in the online issue, which is available at wileyonlinelibrary.com.]

Figure 9. Stabilization of child droplet sizes for different initial parent droplets (a) and filtered results containing only initial primary child droplets (b).
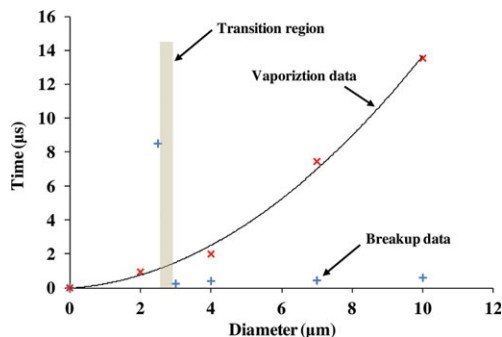
[Color figure can be viewed in the online issue, which is available at wileyonlinelibrary.com.]

between 2.5 and 3 μm, the breakup time increases rapidly. Within this small size range, vaporization suddenly becomes the main driving force for the droplet disintegration.

In Figure 12, the breakup simulation results are presented alongside several different experimental observations showing a good level of agreement in all cases. Figure 12a compares the nondimensional child droplet sizes (d/D_0) with the initial parent droplet We. The experimental observations are taken from Refs. [53–56], and the simulation points plotted include all tested particle sizes from 500 to 2.5 μm. Figure 12b compares the dimensionless time taken to initiate breakup for particles with varying We, where the experimental observations are from Ref. 53 and the four simulation points plotted represent the dimensionless times for droplet sizes: 10, 7, 4, and 3 μm. The 2.5-μm droplet requires a dimensionless time of 60.0 for breakup to initialize, and therefore, resides outside the plotted region. Finally, Figure 12c plots experimentally measured[57] critical Weber number

**Figure 10. Graph showing the rate of decrease in diameter of an evaporating 50 μm droplet.**

Figure 11. Time taken for various sized droplets to either breakup or for their mass to decrease by 10% of their original mass due to vaporization.

[Color figure can be viewed in the online issue, which is available at wileyonlinelibrary.com.]

We_{crit} against the droplet Ohnesorge number. These results are compared to the simulation breakup of the small droplets: 10, 7, 4, 3, and 2.5 μm.

As Figure 12a illustrates, the child droplet sizes predicted by the wave breakup model are in close agreement with the experimental observations. Although TAB breakup simulation results lie outside the experimental data range, their sizes follow a logical trend alongside the wave breakup model. As exhibited, a maximum dimensionless child droplet size ratio exists in the region of the 2.5 and 3 μm parent droplets, with corresponding We of 10.5 and 12.6, respectively. Figure 12b illustrates how the time required to initiate breakup, as predicted by the TAB model, increases continuously with decreasing We number. For droplets below 3 μm and We less than 12.6, the time required increases rapidly. Both the experimental and simulation results presented in Figure 12c are in agreement with Figure 12b, indicating that when the droplet size is reduced below 2.5 μm We falls below We_{crit} of roughly 12, resulting in exponential increases in breakup initiation times.

It is evident that the disintegration process of a water droplet between 50 and 500 μm injected into a HVOF-type system is dependant on both aerodynamic breakup and vaporization to varying degrees; and depends on the droplet fragmentation sizes produced. The respective mass-weighted average diameters of the primary child droplets shed from the 50, 100, 200, and 500 μm parent droplets are 4.403, 4.149, 3.798, and 3.342, respectively. The transition region highlighted in Figure 11 marks the region in which the vaporization mode becomes the dominant form of disintegration process. Looking back at Figure 9b, for a 200-μm parent droplet,
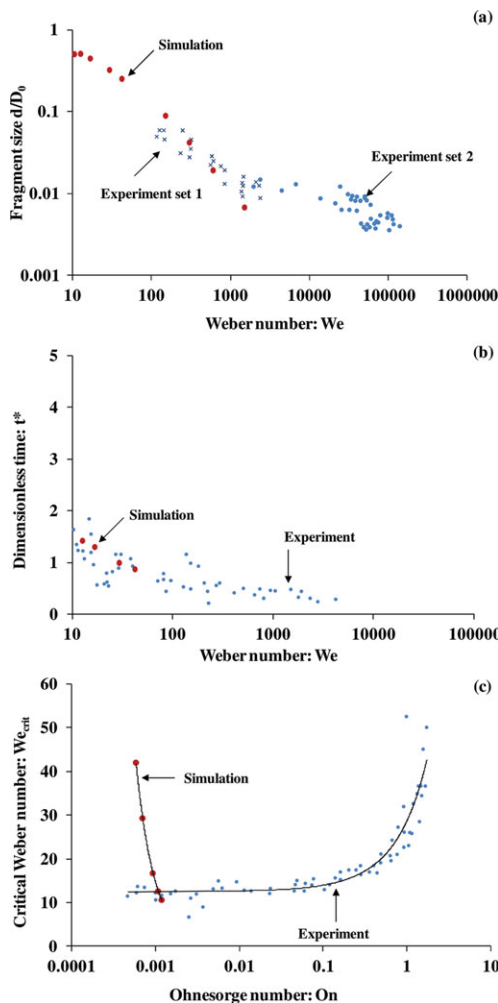
Figure 12. Comparisons between simulations and experimental observation: Time to initiate break up (a), child droplet sizes (b), and the critical We (c).

[Color figure can be viewed in the online issue, which is available at wileyonlinelibrary.com.]

the smallest primary child droplets are close to the transition boundary, whereas for a 500-μm parent droplet roughly half of the primary child droplets reside within the transition zone. As a result, for an initial parent droplet smaller than 200 μm, the disintegration process for its primary child droplets is governed by breakup only. The resulting secondary child droplets then vaporize without breakup. For an initial parent droplet greater than 200 μm, the disintegration process
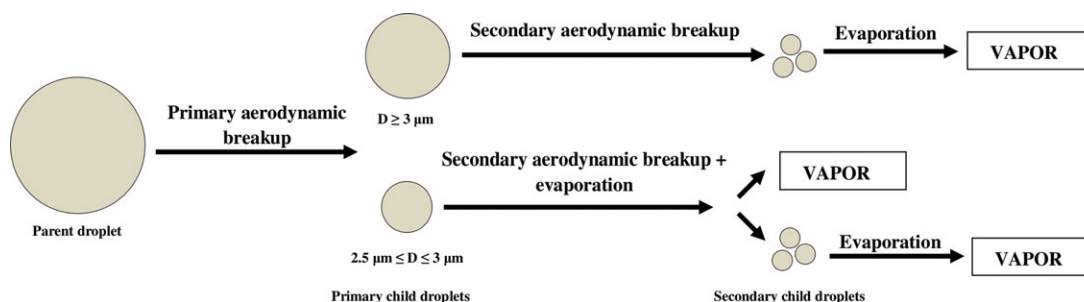
Figure 13. Path diagram showing the different water droplet disintegration routes when injected into a HVOF jet.

[Color figure can be viewed in the online issue, which is available at wileyonlinelibrary.com.]

for its primary child droplets may follow one of two routes. For the child droplets larger than 3 μm, disintegration is governed by aerodynamic breakup only, and then vaporization. For the droplets between 2.5 and 3 μm, disintegration is driven simultaneously by both vaporization and aerodynamic breakup. These investigated droplet disintegration regimes are finally summarized schematically in Figure 13.

The characterized disintegration process may be controlled to some extent, by the predetermined properties of the solution or suspensions being sprayed, and by doing so, the deposition process can be optimized for the spray method at hand.

For instance, fragmentation of the feedstock depends on the Weber (We) and Ohnesorge (Oh) numbers and can be tailored by adjusting the liquid viscosity. For example, in liquid precursor thermal spraying, it has been shown that changing the concentration of 7 wt % yttria-stabilized zirconia from 0.6 to 2.4 mol raises the solution viscosity from 0.0014 to 0.007 Pa S.[58] For suspensions, certain additives such as polyvinyl alcohol can be used to increase the suspension viscosity.[59,60] The suspension solid volume fraction and particle-size distribution influences the suspension viscosity, but to a less extent, and can be expected to raise the viscosity by no more than 50%.[61,62]

In general, the fundamental understanding of liquid feedstock thermal spraying is still in its infancy and the optimum feedstock configurations such as concentrations of solid particles, additives, dispersants, and precursor solutions, as well as the particle-size and size distributions, and type of solvent used for different deposited materials and for different processing methods are not yet fully determined. Furthermore, the levels of experimental data trends for estimating the thermophysical properties such as viscosity, surface tension, specific heat capacity, and thermal conductivity during the complete liquid disintegration process are limited. The results presented serve as a baseline study for liquid feedstock injection using detailed water properties to study the liquid droplet disintegration process. The insight gained from the study is a useful step forward in the understanding and on going developments of liquid feedstocks in thermal spraying.

Conclusions and Future Work

The disintegration process of water droplets between 50 and 500 μm entering a HVOF-type system are simulated and the breakup time scales and droplet sizes compare well to experimental observations. The results obtained indicate that the droplet disintegration process is dependant on the initial parent droplet sizes. An initial parent droplet between 50 and 200 μm in size will breakup, forming droplets which then vaporizes. For a parent droplet between 200 and 500 μm, a fraction of the child droplets will undergo vaporization, and a fraction will undergo further breakup and simultaneous vaporization.

Acknowledgments

Notation

General symbols

A_p = surface area of a particle
A_0 = constant in realizable k-ε model (4.04)
A_s = constant in eddy dissipation model (4.0)
a = decreasing parent droplet radius
B_0 = wave breakup model constant
B_1 = wave breakup model constant
C_1 = constant for the linear pressure strain model (1.8)
$C_{1\varepsilon}$ = constant for the turbulent dissipation of energy (1.44)
C_2 = constant for the linear pressure strain model (0.6)
$C_{2\varepsilon}$ = constant for the turbulent dissipation of energy (1.92)
C_D = Drag coefficient
C_p = specific heat capacity at constant pressure
C_b = TAB model constant (0.5)
C_d = TAB model constant (5)
C_F = TAB model constant (1/3)
C_k = TAB model constant (8)
d_p = particle diameter
$D_{i,m}$ = diffusion coefficient of water vapor in the bulk flow
E = total energy
F = additional force term
G_b = generation of turbulence energy due to buoyancy
G_k = generation of turbulence energy due to mean velocity gradients
h = convective heat-transfer coefficient
h_{fg} = enthalpy of vaporization
K = thermal conductivity
k = turbulent kinetic energy
k_c = mass-transfer coefficient
m = mass
M = Mach number
$M_{\omega,i}$ = molecular weight of species i
N_i = molar flux of vapor
Nu = Nusselt number
Oh = Ohnesorge number
P = pressure
Pr = Prandtl number
P_{sat} = saturated pressure
r = radial distance from centerline
r_p = particle radius
r_{32} = Sauter mean radius of the droplet size distribution
$R_{i,r}$ = net rate of production of species i due to reaction r
R = universal gas constant
Re = Reynolds number
S = molecular speed ratio
Sc = Schmidt number
S_m = mass source term
Ta = Taylor number
t = Time
T = Temperature
u_p = particle velocity
v = gas-phase velocity
v_{rel} = relative velocity magnitude between the gas phase and discrete droplet
$v'_{i,r}$ = stoichiometric coefficient for reactant i in reaction r
$v_{j,r}$ = stoichiometric coefficient for product i in reaction r
We = Weber number
X_i = local bulk mole fraction
Y = local bulk mass fraction
y = nondimensional distortion
Y_M = contribution of the fluctuating dilatation in compressible turbulence to dissipation rate
Z = ratio of total energy in distortion and oscillation to the energy in the fundamental mode

Greek letters

ε = turbulent kinetic energy dissipation rate
μ = dynamic viscosity
ρ = density
σ = particle surface tension
Λ = wavelength of most unstable wave on droplet surface
τ_p = particle breakup time
Ω = maximum growth rate for the droplet surface instability waves
υ = kinematic viscosity
σ_k = turbulent Prandtl number for k
σ_ε = turbulent Prandtl number for ε

Subscripts

eff = sum of the physical and turbulent values
i = referring to one of many species
p = particle

r = radial coordinate direction
R = reactant
t = thermophoretic
x = axial coordinate direction
∞ = free stream conditions

Mathematical operators

∂ = partial differential
∇ = Del operator
Δ = difference between two quantities of a variable
$\vec{v}$ = vector form of variable
$\dot{v}$ = time derivative
$\ddot{v}$ = double time derivative

Literature Cited

1. Fauchais P, Vardelle A. Innovative and emerging processes in plasma spraying: from micro- to nano-structured coatings. *J Phys D: Appl Phys*. 2011;44:1–14.
2. Kumar A, Bae G, Kang K, Yoon S, Lee C. Effect of powder state on the deposition behaviour and coating development in kinetic spray process. *J Phys D: Appl Phys*. 2009;42:1–8.
3. Yoon S, Xiong Y, Kim H, Lee C. Dependence of initial powder temperature on impact behaviour of bulk metallic glass in a kinetic spray process. *J Phys D: Appl Phys*. 2009;42:1–5.
4. Li M, Christophides PD. Modelling and control of high-velocity oxygen-fuel (HVOF) thermal spray: a tutorial review. *J Therm Spray Technol*. 2009;18:753–768.
5. O'Regan B, Grätzel M. A low-cost, high-efficiency solar cell based on dye-sensitized colloidal TiO_2 films. *Nature*. 1991;353:737–740.
6. Bai X, More K, Rouleau CM, Rabiei A. Functionally graded hydroxyapatite coating doped with antibacterial components. *Acta Biomater*. 2010;6:2264–2273.
7. Fauchais P, Montavon G, Lima R, Marple BR. Engineering a new class of thermal spray nano-based microstructures from agglomerated nanostructured particles, suspensions and solutions: an invited review. *J Phys D: Appl Phys*. 2011;44:1–53.
8. Killinger A, Gadow R, Mauer G, Guignard A, Vaßen R, Stöver D. Review of new developments in suspension and solution precursor thermal spray processes. *J Therm Spray Technol*. 2011;20:677–695.
9. Fauchais P, Montavon G. Latest developments in suspension and liquid precursor thermal spraying. *J Therm Spray Technol*. 2010; 19:226–239.
10. Pawlowski L. Suspension and solution thermal spray coatings. *Surf Coat Technol*. 2009;203:2807–2829.
11. Pawlowski L. Finely grained nanometric and submicrometric coatings by thermal spraying: a review. *Surf Coat Technol*. 2008;202: 4318–4328.
12. Huang Y, Song L, Liu X, Xiao Y, Wu Y, Chen J, Wu F, Gu Z. Hydroxyapatite coatings deposited by liquid precursor plasma spraying: controlled dense and porous microstructures and osteoblastic cell responses. *Biofabrication*. 2010;2:1–10.
13. Vaßen R, Yi Z, Kaßner H, Stöver D. Suspension plasma spraying of TiO_2 for the manufacture of photovoltaic cells. *Surf Coat Technol*. 2009;203:2146–2149.
14. Toma F-L, Berger L-M, Stahr CC, Naumann T, Langner S. Microstructures and functional properties of suspension-sprayed Al_2O_3 and TiO_2 coatings: an overview. *J Therm Spray Technol*. 2010;19:262–274.
15. Bonini M, Bardi U, Berti D, Neto C, Baglioni P. A new way to prepare nanostructured materials: flame spray of microemulsions. *J Phys Chem B*. 2002;106:6178–6183.
16. Mäkelä JM, Keskinen H, Forsblom T, Keskinen J. Generation of metal and metal oxide nanoparticles by liquid flame spray process. *J Mater Sci*. 2004;39:2783–2788.
17. Heine MC, Pratsinis SE. Droplet and particle dynamics during flame spray synthesis of nanoparticles. *Ind Eng Chem Res*. 2005;44:6222–6232.
18. Li C-J, Yang G-J, Wang Z. Formation of nanostructured TiO_2 by flame spraying with liquid feedstock. *Mater Lett*. 2003;57:2130–2134.
19. Yang G-J, Li C-J, Wang Y-Y. Phase formation of nano-TiO_2 particles during flame spraying with liquid feedstock. *Therm Spray Technol*. 2005;14:480–486.
20. Killinger A, Kuhn M, Gadow R. High-velocity suspension flame spraying (HVSFS), a new approach for spraying nanoparticles with hypersonic speed. *Surf Coat Technol*. 2006;201:1922–1929.
21. Bolelli G, Rauch J, Cannillo V, Killinger A, Lusvarghi L, Gadow R. Microstructural and tribological investigation of high-velocity suspension flame sprayed (HVSFS) Al_2O_3 coatings. *J Therm Spray Technol*. 2009;18:35–49.
22. Oberste-Berghaus J, Legoux J-G, Moreau C, Hui R, Decès-Petit C, Qu W, Yick S, Wang Z, Maric R, Ghosh D. Suspension and HVOF spraying of reduced temperature solid oxide fuel cell electrolytes. *J Therm Spray Technol*. 2008;17:700–707.
23. Meillot E, Vert R, Caruyer C, Damiani D, Vardelle M. Manufacturing of nanostructured YSZ coatings by suspension plasma spraying (SPS): effect of injection parameters. *J Phys D: Appl Phys*. 2008;44:1–8.
24. Basu S, Cetegen BM. Modelling of thermo-physical processes in liquid ceramic precursor droplets injected into a plasma jet. *Int J Heat Mass Transfer* 2007;50:3278–3290.
25. Basu S, Cetegen BM. Modeling of liquid ceramic precursor droplets in a high velocity oxy-fuel flame jet. *Acta Mater*. 2008;56:2750–2759.
26. Gadow R, Killinger A, Rauch J. New results in high velocity suspension flame spraying (HVSFS). *Surf Coat Technol*. 2008;202:4329–4336.
27. Tikkanen J, Gross KA, Berndt CC, Pitktnen V, Keskinen J, Raghu S, Rajala M, Karthikeyan J. Characteristics of the liquid flame spray process. *Surf Coat Technol*. 1997;90:210–216.
28. Tabbara H, Gu S. Computational simulation of liquid-fuelled HVOF thermal spraying. *Surf Coat Technol*. 2009;204:676–684.
29. Tabbara H, Gu S. Computational modelling of titanium particles in warm spray. *Comput Fluids*. 2011;44:358–368.
30. Tabbara H, Gu S, McCartney DG, Price TS, Shipway PH. Study on process optimization of cold gas spraying. *J Therm Spray Technol*. 2010;20:608–620.
31. Li M, Christofides PD. Multiscale modeling and analysis of an industrial HVOF thermal spray process. *Chem Eng Sci*. 2005;60:3649–3669.
32. Shi D, Li M, Christofides PD. Diamond jet hybrid HVOF thermal spray: rule-based modeling of coating microstructure. *Ind Eng Chem Res*. 2004;43:3653–3665.
33. Li M, Shi D, Christofides PD. Diamond jet hybrid HVOF thermal spray: gas-phase and particle behavior modeling and feedback control design. *Ind Eng Chem Res*. 2004;43:3632–3652.
34. Van Doormal JP, Raithby GD, McDonald BH. The segregated approach to predicting viscous compressible fluid flows. *J Turbomach*. 1987;109:268–277.
35. Peric M. Analysis of pressure–velocity coupling on non-orthogonal grids. *Numer Heat Transfer Part B*. 1990;17:63–82.
36. Raithby GD, Schneider GE. Numerical solution of problems in compressible fluid flow: treatment of the velocity–pressure coupling. *Numer Heat Transfer*. 1979: 2; 417–440.
37. Magnussen BF, Hjertager BH. On mathematical models of turbulent combustion with special emphasis on soot formation and combustion. *Int Symp Combust*. 1977;16:719–729.
38. Launder BE, Spalding DB. *Lectures in Mathematical Models of Turbulence*. London: Academic Press, 1972.
39. Shih TH, Liou WW, Shabbir A, Zhu J. A new eddy viscosity model for high Reynolds number turbulent flows. *Comput Fluids*. 1995;24:227–238.
40. Crowe C, Sommerfeld M, Tsuji Y. *Multiphase Flows With Droplets and Particles*. Boca Raton: CRC Press, 1998:73.
41. Henderson CB. Drag coefficients of spheres in continuum and rarefied flows. *AIAA J*. 1976;14:707–708.
42. Ranz WE, Marshall WR. Evaporation from drops (part I). *Chem Eng Prog*. 1952;48:141–146.
43. Ranz WE, Marshall WR. Evaporation from drops (Part II). *Chem Eng Prog*. 1952;48:173–180.
44. Touloukian YS. *Specific Heat: Nonmetallic Liquids and Gases Thermophysical Properties of Matter TPRS Data Series*. The University of Michigan: IFI/Plenum, 1970. p. 102.
45. Cengal YA, Boles M. *Thermodynamics: An Engineering Approach*, 4th ed. New York: McGraw-Hill, 2002:610–612.
46. Bird RB. *Transport phenomena*. USA: Wiley. 1960. p. 505.
47. Reitz RD. Mechanisms of atomization processes in high-pressure vaporizing sprays. *Atom Spray Technol*. 1987;3:309–337.
48. Deguchi S, Ghosh SK, Alargova RG, Tsujii K. Viscosity measurements of water at high temperatures and pressures using dynamic light scattering. *J Phys Chem B*. 2006;110:18358–18362.
49. Kestin J, Sengers JV, Kamgar-Parsi B, Levelt Sengers JMH. Thermophysical properties of H_2O. *J Phys Chem Ref Data*. 1984;13:175–183.
50. Taylor GI. *The shape and acceleration of a drop in a high speed air stream*. Technical report, The Scientific Papers of G.I. Taylor, Vol. 3, ed., G.K. Batchelor. University Press Cambridge, 1963.
51. Hackett CM, Settles GS. *The influence of nozzle design on HVOF spray particle velocity and temperature*. In: Berndt CC, Sampath S, editors. *1995 Advances in Thermal Spray Science & Technology,*

Proceedings of the 8th National Thermal Spray Conference. Materials Park, OH: ASM International, 1995.

52. Swank WD, Fincke JR, Haggard D, Irons G. *HVOF gas flow field characteristics*. In: Berndt CC, Sampath S, editors. *Thermal Spray Industrial Applications, Proceedings of the 7th National Thermal Spray Conference*. Materials Park, OH: ASM International, 1994.

53. Wolfe HE, Anderson WH. Kinetics, mechanism, and resultant droplet sizes of the aerodynamics breakup of liquid drops. AGCD Report No. 0395-04 (18) SP, Aerojet General Corp., Downey, California. 1964.

54. Lane WR, Prewett WC, Edwards J. Some Experiments on the Shatter of Drops by Transient Blasts of Air. Technical Paper No. 115, Serial 15, Porton, England. 1949.

55. Lane WR. Shatter of drops in stream of air. *Ind Eng Chem*. 1951;43:1312–1337.

56. Lane WR, Dorman RG. Further experiments on the shattering of drops by a supersonic air blast. Technical paper No. 279, Porton, England. 1952.

57. Haas FC. Stability of droplets suddenly exposed to a high velocity gas stream. *AICHE J*. 1964;10:920–924.

58. Chen D, Jordan EH, Gell M. Effect of solution concentration on splat formation and coating microstructure using the solution precursor plasma spray process. *Surf Coat Technol*. 2008;202:2132–2138.

59. Rampon R, Toma F-L, Bertrand G, Coddet C. Liquid plasma sprayed coatings of yttria-stabilized zirconia for SOFC electrolytes. *J Therm Spray Technol*. 2006;15:682–688.

60. Rampon R, Filiatre C, Bertrand G. Suspension plasma spraying of YPSZ coatings: suspension atomization and injection. *J Therm Spray Technol*. 2008;17:105–114.

61. Roscoe R. The viscosity of suspensions of rigid spheres. *Br J Appl Phys*. 1952;3:267–269.

62. Nguyen CT, Desgranges F, Galanis N, Roya G, Maréd T, Boucher S, Angue Mintsa HA. Viscosity data for Al_2O_3–water nanofluid—hysteresis: is heat transfer enhancement using nanofluids reliable? *Int J Therm Sci*. 2008;47:103–111.